Biomaterials 302 (2023) 122352

Contents lists available at ScienceDirect

Biomaterials

journal homepage: www.elsevier.com/locate/biomaterials

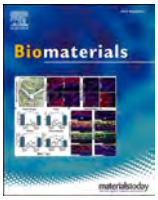

Bio-orthogonal engineered peptide: A multi-functional strategy for the gene therapy of osteoporotic bone loss

Wei Wang [a,1], Qing Wang [a,1], Lei Yu [a,b,1], Gaoran Ge [a], Xin Liu [a], Ang Gao [c], Guomin Wang [d], Zhengwei Wu [d,e], Jiaxiang Bai [a,b,f,***], Huaiyu Wang [c,**], Paul K. Chu [d], Dechun Geng [a,*]

[a] Department of Orthopedics, Medical 3D Printing Center, The First Affiliated Hospital of Soochow University, 188 Shizi Road, Suzhou, 215006, Jiangsu, China
[b] Department of Orthopedics, The First Affiliated Hospital of USTC, Division of Life Sciences and Medicine, University of Science and Technology of China, Hefei, 230022, China
[c] Center for Human Tissues and Organs Degeneration, Shenzhen Institute of Advanced Technology, Chinese Academy of Sciences, Shenzhen, 518055, China
[d] Department of Physics, Department of Materials Science and Engineering, And Department of Biomedical Engineering, City University of Hong Kong, Tat Chee Avenue, Kowloon, Hong Kong, China
[e] School of Nuclear Science and Technology and CAS Key Laboratory of Geospace Environment, University of Science and Technology of China, Hefei, China
[f] National Center for Translational Medicine (Shanghai) SHU Branch, Shanghai University, Shanghai, China

ARTICLE INFO

Keywords:
Gene therapy
Bio-orthogonal chemistry
Osteoporosis and osteoporotic fractures
Osteoclasts
Reactive oxygen species

ABSTRACT

Osteoporosis is a degenerative disease affecting millions of elderly people globally and increases the risk of bone fractures due to the reduced bone density. Drugs are normally prescribed to treat osteoporosis, especially after surgical treatment of osteoporotic fractures. However, many anti-osteoporotic drugs produce deleterious side effects. The recent development of gene therapy utilizing oligonucleotides (ONs) has spurred the development of new therapies for osteoporosis. Nevertheless, most ONs lack the capability of cell penetration and lysosome escape and hence, intracellular delivery of ON remains a challenge. Herein, a novel strategy is demonstrated to efficiently deliver ON to cells by combining ON with the cell-penetrating peptide (CPP) *via* the bio-orthogonal click reaction. Several dopamine (DOPA) groups are also introduced into the fabricated peptide to scavenge intracellular reactive oxygen species (ROS). Owing to favorable properties such as good cytocompatibility, cell penetration, lysosome escape, ROS scavenging, and osteoclastogenesis suppression, the hybrid CPP-DOPA-ON peptide improves the osteoporotic conditions significantly *in vivo* even when bone implants are involved. This strategy has great potential in the treatment of osteoporosis and potentially broadens the scope of gene therapy.

1. Introduction

Osteoporosis is one of the major causes of bone fractures, especially low-energy fractures [1]. The incidence of osteoporosis and osteoporotic fractures increases with age and it is accompanied by a high rate of recurrence and morbidity [2,3]. It is estimated that 47.3 % of women and 23.8 % of men over 50 years old will suffer from osteoporotic fractures during their lifetime and surgical interventions are usually required [4]. Despite the continuous development and improvement of orthopedic implants and surgical techniques, poor bone-implant integration remains one of the main issues after surgery, because the regeneration capability of osteoporotic bone is impaired by problematic quality and quantity [5,6]. Even when the bone implants are surface-modified to produce specific bio-functions, they can only deliver local effects around the implants, but generally fail to alleviate the pathological microenvironment of osteoporosis systemically.

Normal bone homeostasis relies on the dynamic and delicate balance between new bone formation and bone resorption. Under the pathological conditions of osteoporosis, osteoclasts are hyperactive causing faster bone resorption than bone formation mediated by osteoblasts [7,8]. Furthermore, the oxidative stress in the physiological microenvironment is associated with aging and contributes to the development of

* Corresponding author .
** Corresponding author.
*** Corresponding author. Department of Orthopedics, Medical 3D Printing Center, The First Affiliated Hospital of Soochow University, 188 Shizi Road, Suzhou, 215006, Jiangsu, China.
E-mail addresses: jxbai1995@163.com (J. Bai), hy.wang1@siat.ac.cn (H. Wang), szgengdc@suda.edu.cn (D. Geng).
[1] These authors contributed equally to this work.

https://doi.org/10.1016/j.biomaterials.2023.122352
Received 19 August 2023; Received in revised form 7 October 2023; Accepted 12 October 2023
Available online 13 October 2023

osteoporosis [9,10]. When an osteoporotic fracture occurs, healing tends to be difficult. In addition, the disequilibrium of homeostasis under osteoporotic conditions renders the bone-implant interface unstable, eventually leading to implant loosening and even failure. Therefore, restoration of bone homeostasis by inhibiting excessive bone resorption and/or counteracting insufficient bone formation should be the primary goal in the treatment of osteoporosis and osteoporotic fractures. Nevertheless, common first-line drugs for treating osteoporosis are strong antiresorptive ones such as bisphosphonates and denosumab, which tend to increase the risk of atypical fractures and osteonecrosis of the jaw after long-term usage [11,12]. The anabolic regents including parathyroid hormone and parathyroid hormone-related protein are also available for treating osteoporosis but unfortunately, they are expensive and may trigger the occurrence of osteosarcoma [13,14]. In this respect, the development of innovative systemic drug regimens with minimal side effects is imperative for the treatment of osteoporosis. When the oxidative stress regulation is taken into consideration simultaneously, better therapeutic effects may be achieved.

Recent development and application of gene therapy bring new hope to the treatment of osteoporosis [15,16]. Notably, therapeutics utilizing microRNA (miRNA) or small interfering RNA (siRNA) have the advantage of regulating specific functional proteins rather than affecting the whole genetics in the host boding well for osteoporosis therapy [17–20]. However, efficient delivery of oligonucleotides (ON) into cells and tissues is a challenging task, as exogenetic ON is readily cleared by the human defense system in addition to electrostatic repulsion between ON and cell membranes with a negative charge. Furthermore, the delivered ON should timely and efficiently escape from the endolysosomal system of cells into cytoplasm prior to lysosomal degradation or re-export *via* exocytosis [15,21,22]. Therefore, new delivery strategies with biosafety should be developed to improve the therapeutic effects of ON for osteoporosis treatment.

In this study, the ON for treating osteoporosis is combined with cell penetrating peptide (CPP) and dopamine (DOPA) to achieve better therapeutic effects. A single ON strand (UUCUACCAUUGCCAA) is selected as the major functional sequence because it can provide the osteo-protective effect by specifically inhibiting miRNA-182 (a miRNA capable of promoting osteoclastogenesis *via* the suppression of autocrine IFN-β pathway) [23,24]. As a kind of CPP, arginine-rich short peptide (RRRRRRRRR) that can efficiently penetrate the cell membrane and escape from lysosomes without causing cytotoxicity is adopted in our study. In order to realize oxidative stress regulation, several DOPA groups with antioxidant properties are further introduced into the fragment of peptide [25]. The ON strand and CPP-DOPA peptide are modified with the Azido group and dibenzocyclooctane (DBCO) group respectively, to enable their specific conjugation with a ratio of 1:1 *via* the classical bio-orthogonal click reaction [26,27]. The CPP-DOPA-ON peptide not only enters the cells efficiently, but also allows scavenging of intracellular reactive oxygen species (ROS) to complement gene therapy. Our study reveals a new therapy and provides insights into the treatment of osteoporosis, especially for the postsurgical rehabilitation of osteoporotic fractures (Scheme 1).

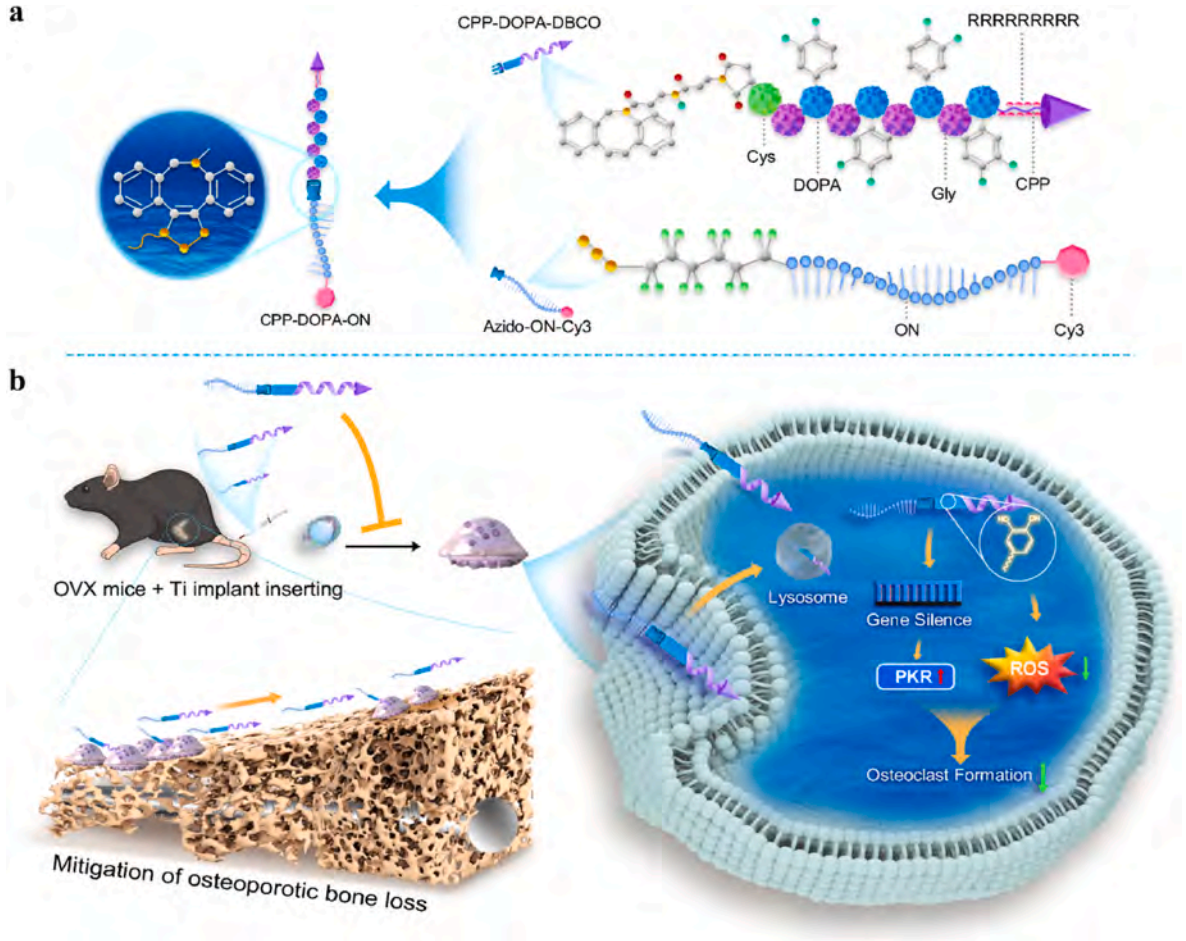

Scheme 1. Schematic illustration of the fabrication of CPP-DOPA-ON with multi-functions. (a) Arginine-rich short peptide (RRRRRRRRR) modified with DOPA and DBCO motifs grafted with the single ON strand with the Azido end group *via* the bio-orthogonal click reaction; (b) Hybrid CPP-DOPA-ON peptide enables high-efficiency delivery of ON into cells and scavenging of intracellular ROS desirable for the treatment of osteoporosis and poor bone-implant integration under osteoporotic conditions.

2. Materials and methods

2.1. Materials

Dopamine was purchased from Sigma-Aldrich (USA) and murine RANKL was supplied by from R&D Systems (USA). Dulbecco's modified Eagle's medium (DMEM, high glucose) and fetal bovine serum (FBS) were bought from VivaCell (China). The CCK-8 assay kits and live/dead cell staining kits were obtained from Yeasen (China) and the Urea-PAGE Preparation Kit, LysoTracker Green, ALP staining kit, ARS staining kit, TRIzol reagent, and dihydroethidium (DHE) staining kit were provided by Beyotime (China). The TRAP staining kit was obtained from Bizhong Bio (China). The primary antibodies NFATc1 (A1539), c-fos (A16641), CTSK (A1782) and Nrf2 (A0674) were obtained from ABclonal (China) and HO-1 (ab189491) and SOD2 (ab137037) were obtained from Abcam (UK). The HRP Goat Anti-Rabbit Secondary Antibody (AS014) was obtained from ABclonal (China).

2.2. Synthesis

CPP-DOPA-DBCO, Azido-ON, and Azido–ON–Cy3 were prepared in collaboration with ChinaPeptides Co., Ltd. (QYAOBIO, China) according to the methods described previously. CPP-DOPA-ON and CPP-DOPA–ON–Cy3 were fabricated by mixing CPP-DOPA-DBCO with Azido-ON or Azido–ON–Cy3 in aqueous solutions with a molar ratio of 1:1 and then kept at 4 °C.

2.3. Characterization

CPP-DOPA-DBCO was analyzed by ESI-MS on the ThermoFisher LTQ XL™ Mass Spectrometer (ThermoFisher, USA), and Azido-ON and Azido–ON–Cy3 were analyzed by ESI-MS on the AB SCIEX API 150EX™ LC/MS System (AB SCIEX, USA). The ^{1}H NMR spectra were acquired from CPP-DOPA-DBCO on the Bruker DRX500 spectrometer and 15 % urea polyacrylamide gel electrophoresis (Urea-PAGE) was carried out to verify the fabrication of CPP-DOPA-ON and CPP-DOPA–ON–Cy3.

2.4. Cytotoxicity

The murine-derived RAW264.7 cells were purchased from the National Collection of Authenticated Cell Cultures of China and cultured in DMEM supplemented with 10 % (v/v) FBS. The dose-dependent cytotoxicity of CPP-DOPA-DBCO, Azido-ON, and CPP-DOPA-ON to RAW264.7 cells was assessed using the CCK-8 assay. In live/dead cell staining, the cells were seeded on 24-well plates with a density of 60,000 cells/well, cultured overnight to reach adherence, and incubated with 100 nM CPP-DOPA-DBCO, Azido-ON, CPP-DOPA-ON, Lipo, and Lipo/ON for another 24 h. Afterward, the treated cells were co-stained using the live/dead cell staining kits according to manufacturer's instructions. The fluorescence images of live/dead cells were captured by a fluorescence microscope (Zeiss, Germany). After incubating the RAW264.7 cells with 100 nM of CPP-DOPA-DBCO, Azido-ON, and CPP-DOPA-ON for 1 and 3 days, the CCK-8 assay was employed and the optical density (OD) at 450 nm was measured on the microplate reader (BioTek, USA).

2.5. Flow cytometry

The Cy3-labeled samples (Azido–ON–Cy3, CPP-DOPA–ON–Cy3, and Lipo/ON-Cy3) were used to investigate the cellular uptake of RAW264.7 cells under different conditions. The cells were seeded on 12-well plates and cultured overnight to reach adherence. Subsequently, the culture medium was replaced with the medium containing 100 nM Azido–ON–Cy3, CPP-DOPA–ON–Cy3, or Lipo/ON-Cy3. After transfection for 3, 6, 12 and 24 h, the treated cells were washed with PBS 3 times and harvested for flow cytometry (Thermo Fisher, USA). The data were analyzed by the Flow Jo software (Bethesda, USA).

2.6. Lysosome escape

The RAW264.7 cells were seeded on slides on 24-well plates with a density of 30,000 cells/well and cultured overnight to reach adherence. The culture medium was replaced with the serum-free medium containing 100 nM CPP-DOPA–ON–Cy3 and incubated for another 6 or 12 h. The commercial lysotracker was added to the culture medium to co-stain the cells following the protocol provided by the manufacturer (Beyotime, China). After co-staining for different time periods, fluorescence images were obtained from the cytoplasm of CPP-DOPA–ON–Cy3 (red) and lysotracker (green) by fluorescence microscopy (Zeiss, Germany).

2.7. In vitro osteoclastogenesis

The RAW264.7 cells were seeded on 48-well plates with a density of 30,000 cells/well and cultured overnight to reach adherence. After the different treatments for 12 h, RANKL (50 ng/ml) was added to the culture medium to induce the formation of osteoclasts. Osteoclastic differentiation was evaluated by F-actin staining and TRAP staining according to the manufacturer's instructions. During the F-actin staining of cells using rhodamine, DAPI was used to co-stain the nuclei. The fluorescence images were obtained by fluorescence microscopy (Zeiss, Germany) and the images of the TRAP-positive osteoclasts ($\geq$3 nuclei) were captured on a bright microscope (Zeiss, Germany) and quantified.

2.8. In vitro osteogenesis

The MC3T3-E1 cells were purchased from the National Collection of Authenticated Cell Cultures of China and cultured in DMEM supplemented with 10 % (v/v) FBS. The dose-dependent cytotoxicity of CPP-DOPA-DBCO to MC3T3-E1 cells was assessed using the CCK-8 assay. For the evaluation of *in vitro* osteogenesis, the MC3T3-E1 cells were seeded on 24-well plates with a density of 30,000 cells/well and cultured overnight to reach adherence. After the different treatments (100 nM CPP-DOPA-DBCO, Azido-ON, or CPP-DOPA-ON) for 12 h, the medium was replaced with the osteogenic medium (normal culture medium supplemented with 50 μg ml^{-1} ascorbic acid and 10 mM β-glyceryl phosphate) and cell culturing was performed for 7 days and 14 days, respectively. Finally, osteogenic differentiation was assessed by ALP staining and ARS staining according to the manufacturer's instructions.

2.9. Western blot assays

After the different treatments, the RIPA lysis buffer was used to extract the total cell proteins. Equal amounts of proteins were electrophoresed on polyacrylamide gels and transferred to nitrocellulose membranes. The primary antibodies and secondary antibodies conjugated with horseradish peroxidase were applied successively according to manufacturer's instructions. The relative grey levels of the proteins were examined by enhanced chemiluminescence on the QuickChemi 5200 chemiluminescent imaging system (Monad, China) and ImageJ (Bethesda, USA) was used in the semi-quantitative analysis.

2.10. RNA sequencing

The RAW264.7 macrophages were stimulated by RANKL with or without the CPP-DOPA-ON treatment. The total RNA was extracted from the cells with the TRIzol reagent and RNA sequencing was performed by Genewiz Co. (China). Reads were aligned to the reference genes *via* Hisat2 software and differentially expressed genes remained as the differential fold >1.5 and $p < 0.05$. The KEGG and GO enrichment analyses were performed using DEGs.

2.11. ROS detection

The ROS levels after different treatments were measured by a DHE staining kit according to the manufacturer's instructions. Briefly, the FBS-free medium was added with DHE to culture the cells after the different treatments. Subsequently, the cells were washed with PBS 3 times and observed under a fluorescence microscope (Zeiss, Germany) or analyzed by flow cytometry (Thermo Fisher, USA).

2.12. Animal experiments

The animal experiments were approved by the Animal Ethics Committee of Soochow University (SUDA20220130A01). Twenty-eight 8-week-old female C57BL/6 mice were used and randomly classified into four groups (n = 7/group): Sham group (sham operation + PBS treatment), OVX group (OVX surgery + PBS treatment), Azido-ON group (OVX surgery + Azido-ON treatment) and CPP-DOPA-ON group (OVX surgery + CPP-DOPA-ON treatment). After 4 weeks, the mice underwent Ti implantation on their left femurs. An incision was made along the medial side of the knee joint after disinfection to expose the distal femur. By means of distal femoral metaphysis, the titanium rods (0.5 mm in diameter and 4 mm long) were inserted into the medullary canal of the femur until the implant end was below the articular surface. The patella was relocated and an extensor mechanism was reconstructed. The incision was sutured with penicillin G being given and after 3 days, the mice received administration twice a week for 4 weeks. Finally, all the mice were euthanized and the femurs were collected for the following studies.

2.13. Micro-CT

The bone mass of the distal femurs without implants and new bone formation around the femur implants were measured on the high-resolution SkyScan 1176 micro-CT system (Bruker, Belgium). The scanning parameter was 9 μm per layer, voltage was 50 kV, and current was 200 μA. 3D image reconstruction was then conducted and the bone morphometric parameters including BMD, BV/TV, BS/TV, Tb. N, and Tb. Sp were measured.

2.14. Histological staining

All the collected femurs with or without implants were fixed in 10 % formalin for more than 48 h and decalcified with 10 % EDTA for 30 days. The implanted rods were removed and the specimens were embedded in paraffin wax and cut into 6 μm sections. The morphological changes in the bone tissues were evaluated by H&E staining. TRAP staining and Masson staining were also performed. The histological sections were observed under a bright microscope (Zeiss, Germany), and the number of TRAP-positive polykaryotic osteoclasts in a selected area was quantified.

2.15. TRAP enzyme activity analysis and enzyme-linked immunosorbent assay (ELISA)

After the collection of blood from mice in different groups, the serum was obtained by centrifugation and used for the measurement of TRAP enzyme activity (Beyotime, China) following the manufacturer's instructions. The serum levels of Beta Crosslaps (β-CTx, Elabscience, China) and Procollagen I N-Terminal Propeptide (PINP, Abclonal, China) in mice were also determined by ELISA according to the manufacturer's instructions.

2.16. Statistical analysis

GraphPad Prism version 8.0 was used for the statistical analysis and the data were represented as mean ± standard deviation (SD). The student's *t*-test was conducted for the comparison between two groups and one-way ANOVA was adopted for the comparison among multiple groups. A significant difference was defined at $p < 0.05$ and highly significant difference was defined at $p < 0.01$.

3. Results and discussion

3.1. Materials and characterization

To facilitate the bio-orthogonal click reaction, CPP (RRRRRRRRR) is capped with DOPA and DBCO groups according to previous studies [28, 29]. Meanwhile, Azido-ON is fabricated by linking the Azido group to the miRNA-182 inhibitory sequence (UUCUACCAUUGCCAA) using a spacer of 6 CH_2 units in order to make sure that the Azido group is accessible (Fig. 1a) [23]. To visualize the biological performance of Azido-ON, a Cy3 fluorophore is added to the 3′ end of ON strand to obtain Azido–ON–Cy3. All the synthesized molecules are characterized by electrospray ionization mass spectrometry (ESI-MS). As shown in Fig. 1b, the monoisotopic masses $[M+4H]^{4+}$, $[M+5H]^{5+}$, and $[M+6H]^{6+}$ of CPP-DOPA-DBCO appear at 725.7 Da, 581.2 Da, and 484.4 Da, respectively, which are in line with the theoretical molecular weight of 2899.2 (b). Meanwhile, the monoisotopic masses $[M - 12H]^{12-}$, $[M - 11H]^{11-}$, $[M - 10H]^{10-}$, $[M - 9H]^{9-}$, $[M - 8H]^{8-}$, $[M - 7H]^{7-}$, and $[M - 6H]^{6-}$ of Azido-ON are found at 661.2, 721.3, 793.6, 881.8, 992.3, 1134.2, and 1323.3 Da, respectively, corresponding to the theoretical molecular weight of 7944.6 Da (Fig. 1c). When Azido-ON is modified with the Cy3 fluorophore, the molecular weight increases to 8550.6 Da and hence, $[M - 12H]^{12-}$, $[M - 11H]^{11-}$, $[M - 10H]^{10-}$, $[M -9H]^{9-}$, $[M - 8H]^{8-}$, $[M - 7H]^{7-}$, and $[M - 6H]^{6-}$ of Azido–ON–Cy3 appear at 711.2, 775.9, 853.7, 948.6, 1067.3, 1219.9. and 1423.4 Da, respectively (Fig. 1d). The successful synthesis of CPP-DOPA-DBCO is further demonstrated by ^{1}H nuclear magnetic resonance (^{1}H NMR) spectroscopy, as all the characteristic peaks of CPP-DOPA-DBCO are indicated (Fig. 1e and Fig. S1). High-performance liquid chromatography (HPLC) reveals that all the fabricated samples provide a purity >95 % (Fig. S2). Nondenaturing polyacrylamide gel electrophoresis (PAGE) is further performed to characterize the samples. As shown in Fig. S3, Azido-ON is observed at the lowest position of 25 nt, but after reacting with CPP-DOPA-DBCO, CPP-DOPA-ON shows a slower migration rate due to the larger molecular weight. In contrast, CPP-DOPA-DBCO alone cannot migrate in the gel. A similar phenomenon is observed from Azido–ON–Cy3 and CPP-DOPA–ON–Cy3, and the position of CPP-DOPA–ON–Cy3 is higher than that of CPP-DOPA-ON as expected. In general, the results verify successful fabrication of the different molecules and feasibility of coupling different molecules by the bio-orthogonal click reaction.

3.2. Toxicity evaluation

A low toxicity or nontoxicity is important in clinical applications. To evaluate the risk imposed by possible cell toxicity, different concentrations of CPP-DOPA-DBCO, Azido-ON, and CPP-DOPA-ON are incubated with RAW264.7 macrophages for 2 days and analyzed by the CCK-8 assay. As shown in Fig. 2a–c, no significant toxicity is detected from the molecules despite a large concentration of 1000 nM. The biocompatibility is evaluated by live/dead staining after incubating the RAW264.7 cells with CPP-DOPA-DBCO, Azido-ON, CPP-DOPA-ON, Lipofectamine 2000 (Lipo, a commercial product widely used in oligonucleotide transfection), and Lipofectamine 2000 + Azido-ON (Lipo/ON) for 1 day. CPP-DOPA-DBCO, Azido-ON, and CPP-DOPA-ON have better cytocompatibility than Lipo and Lipo/ON at a concentration of 100 nM, as manifested by less dead cells with red fluorescence (Fig. 2d). The RAW264.7 cells are incubated with 100 nM CPP-DOPA-DBCO, Azido-ON and CPP-DOPA-ON for 1 day and 3 days to monitor cell proliferation. As shown in Fig. 2e, there is no significant difference among the various groups and the concentration of CPP-DOPA-ON is

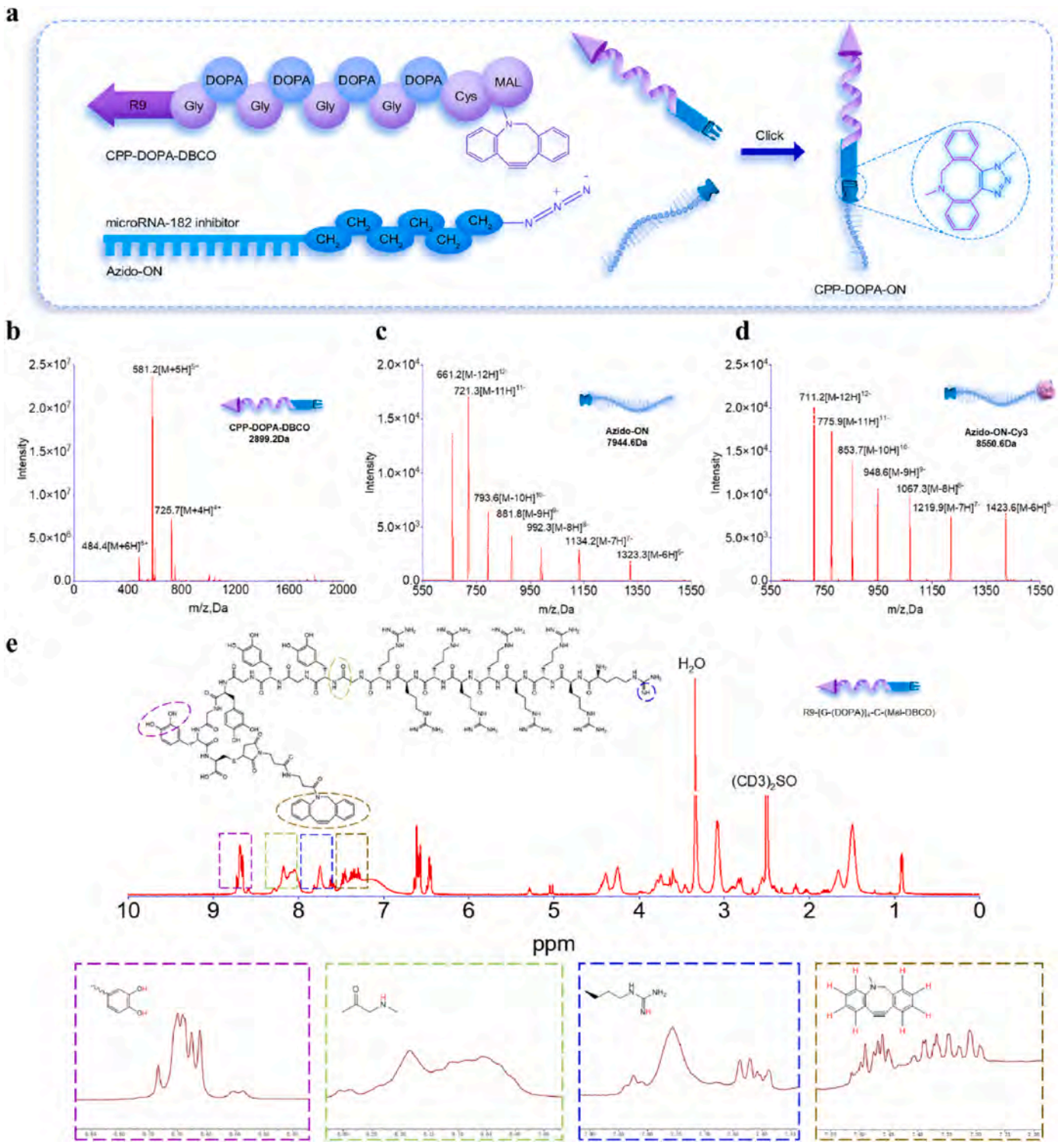

Fig. 1. Characterization results. (a) Molecular structures of CPP-DOPA-DBCO, Azido-ON and CPP-DOPA-ON; (b–d) ESI-MS results of CPP-DOPA-DBCO, Azido-ON and Azido–ON–Cy3; (e) ^{1}H NMR spectrum of CPP-DOPA-DBCO.

thus chosen to be 100 nM in the following *in vitro* studies. The erythrocyte hemolysis assay is adopted to evaluate the hemocompatibility of different samples [30]. In contrast to the results obtained from the positive control, no obvious erythrocyte hemolysis is found from CPP-DOPA-DBCO, Azido-ON, and CPP-DOPA-ON (Fig. 2f and g). These results provide evidence that the biocompatibility of CPP-DOPA-ON is sufficient.

3.3. Dynamic tracing of CPP-DOPA-ON in macrophages

With regard to efficient delivery of the target gene, the cell membrane and lysosomal membrane are two intractable barriers that need to overcome. After crossing the cell membrane by endocytosis, the delivered gene should escape timely and efficiently from the lysosomes into the cytoplasm to exert biological effects. In this respect, the intracellular dynamic trajectory of CPP-DOPA-ON labeled with fluorescent Cy3 is

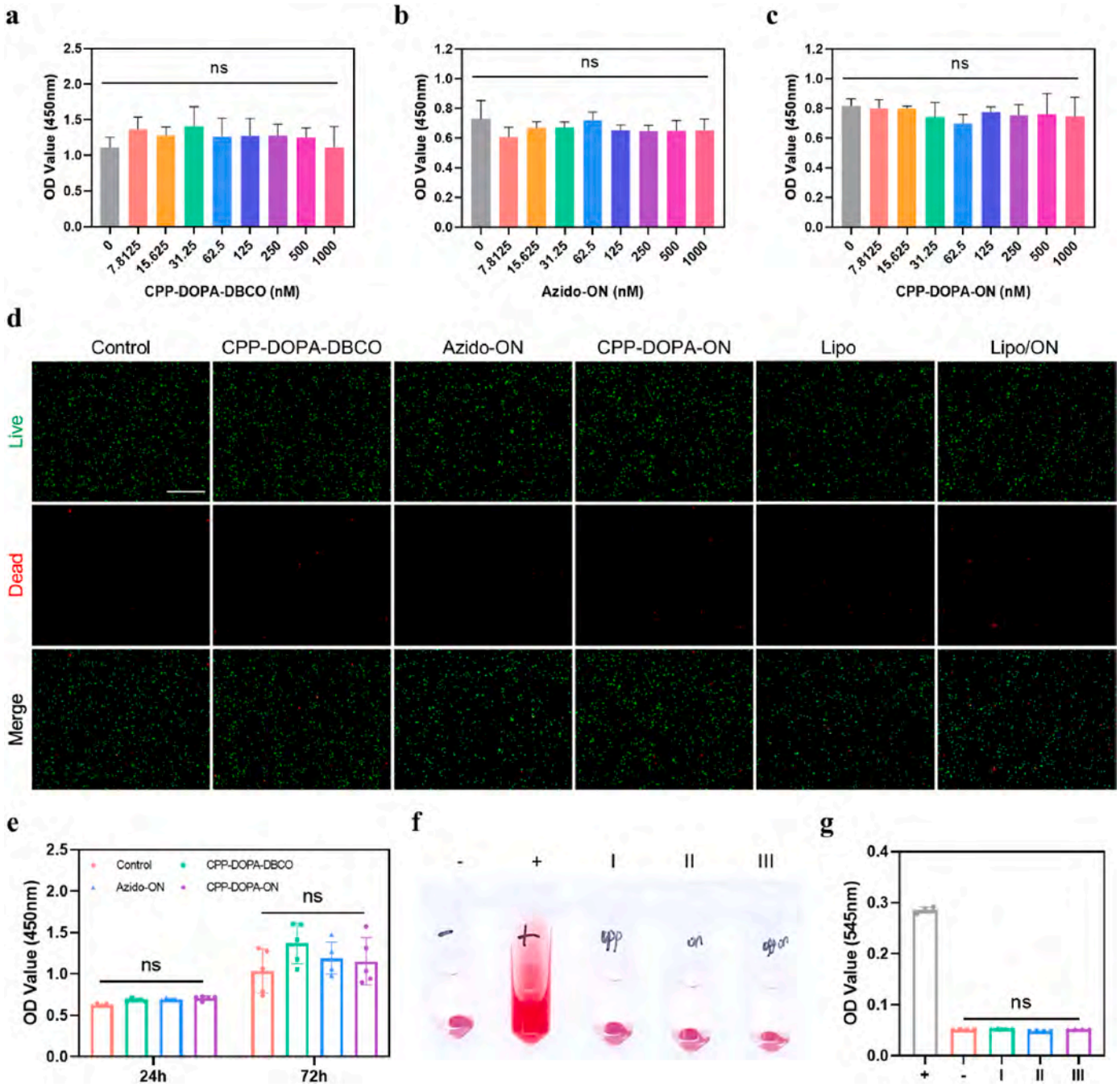

Fig. 2. *In vitro* biocompatibility of CPP-DOPA-ON. (a–c) Viability of RAW264.7 macrophages after incubation with CPP-DOPA-DBCO, Azido-ON, and CPP-DOPA-ON at different concentrations (0–1000 nM) for 2 days; (d) Live & dead staining of RAW264.7 macrophages after incubation with CPP-DOPA-DBCO, Azido-ON, CPP-DOPA-ON, Lipo, and Lipo/ON at a concentration of 100 nM for 1 day, scale bar = 400 μm; (e) Viability of RAW264.7 macrophages after incubation with CPP-DOPA-DBCO, Azido-ON, and CPP-DOPA-ON at a concentration of 100 nM for 1 and 3 days; (f and g) Levels of erythrocyte hemolysis and quantitative analysis after different treatments: Negative control (−), Positive control (+), CPP-DOPA-DBCO (I), Azido-ON (II), CPP-DOPA-ON (III), and ns denotes no significance.

monitored prior to functional verification (Fig. 3a). CPP-DOPA–ON–Cy3 with red fluorescence phagocytosed by RAW264.7 cells is examined dynamically by fluorescence microscopy. As shown in Fig. 3b and Fig. S4, the intracellular fluorescence intensity of Cy3 increases gradually with treatment time indicative of the entrance and accumulation of CPP-DOPA–ON–Cy3 in the cells. After 3, 6, 12 and 24 h of different treatments, the macrophages are analyzed by flow cytometry. Fig. 3c shows that CPP-DOPA–ON–Cy3 has the extraordinary cell penetration ability, as more than 60 % of the cells can be detected within 3 h. In the meantime, the cellular uptake rate of Lipo/ON-Cy3 is only 43.7 %. When the treatment time is extended from 6 h to 24 h, CPP-DOPA–ON–Cy3 also shows better cell penetration than Lipo/ON-Cy3 (Fig. 3c and d). The lysosomal escape capability of CPP-DOPA–ON–Cy3 is further investigated by co-staining the cells in different groups with the commercial lysotracker. As shown in Fig. 3e, after co-incubation for 6 h, the red emission from Cy3 in the cells overlaps the green fluorescence from the commercial lysotracker with a Pearson correlation coefficient (Rr) of 0.78. As the co-incubation time is increased, the intracellular fluorescence intensity of CPP-DOPA–ON–Cy3 increases gradually and some of them migrate to the cytoplasm with Rr decreasing to 0.49 after 12 h (Fig. 3e). All in all, CPP-DOPA–ON–Cy3 has both the cell penetration ability and lysosomal escape ability, which can facilitate the delivery of

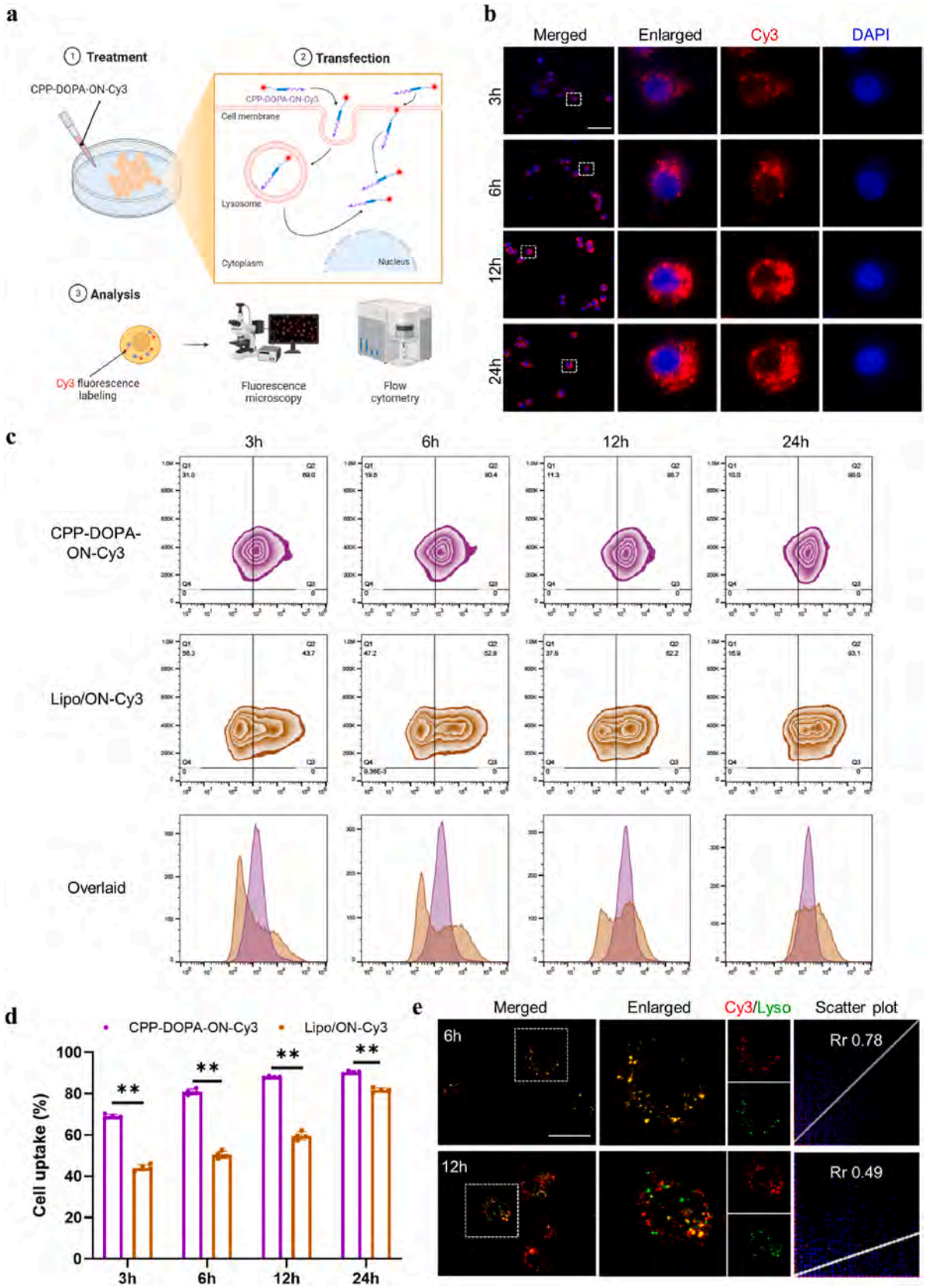

Fig. 3. Dynamic tracing of CPP-DOPA-ON in macrophages. (a) Schematic illustration of the experiments; (b) Fluorescence images of living macrophages treated with CPP-DOPA–ON–Cy3 for 3, 6, 12 and 24 h, scale bar = 50 μm; (c) Flow cytometric analysis of the cells treated with CPP-DOPA–ON–Cy3 or Lipo/ON-Cy3 for 3, 6, 12 and 24 h; (d) Quantitative analysis of the transfected cells shown in (c); (e) Representative fluorescence images and Pearson correlation coefficient of macrophages co-incubated with CPP-DOPA–ON–Cy3 and commercial lysotracker for 6 and 12 h, scale bar = 20 μm and ** denotes $p < 0.01$.

ON to cells and enhance the biological functions thereafter.

3.4. *In vitro* effects of CPP-DOPA-ON

The effects of CPP-DOPA-ON on osteoclastogenesis are evaluated *in vitro*. After the different treatments for 12 h, the macrophages are induced by RANKL to form osteoclasts and the F-actin ring formation of osteoclasts is determined by phalloidin staining. As shown in Fig. 4a–c, CPP-DOPA-ON provides excellent effects on osteoclastogenesis suppression, as the average F-actin area and number detected are even comparable to those of the Lipo/ON group. The tartrate-resistant acid phosphatase (TRAP) staining images show that the formation of TRAP-positive multinucleated osteoclasts is inhibited after the CPP-DOPA-ON treatment (Fig. 4d and e), consistent with the results obtained by the TRAP activity analysis (Fig. 4f). As shown in Fig. 4g and h, the CPP-DOPA-ON treatment down-regulates the levels of the key

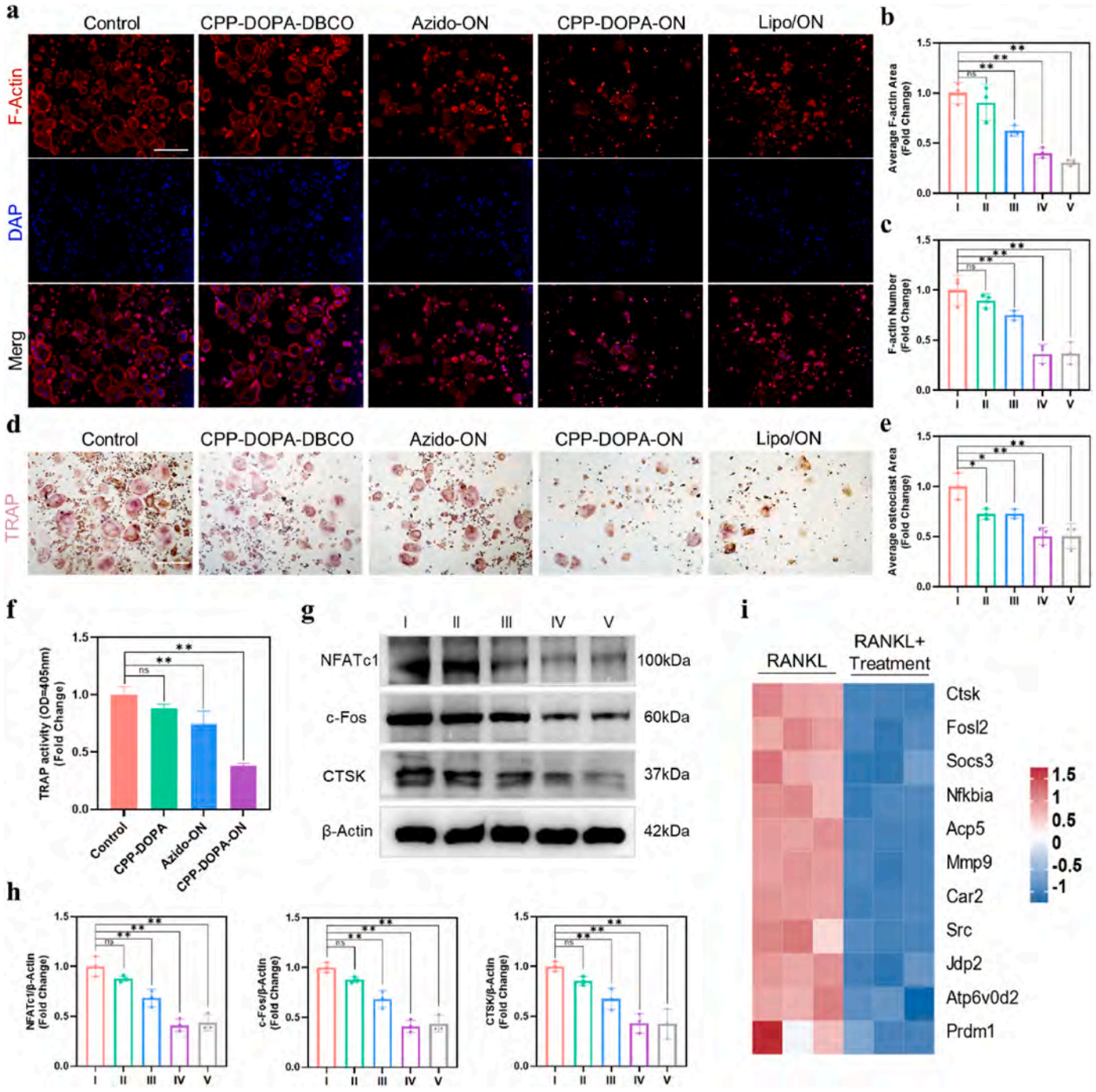

Fig. 4. *In vitro* osteoclastogenesis after different treatments (I: RAW264.7 macrophages after RANKL stimulation, II: RAW264.7 macrophages after RANKL stimulation + CPP-DOPA-DBCO treatment, III: RAW264.7 macrophages after RANKL stimulation + Azido-ON treatment, IV: RAW264.7 macrophages after RANKL stimulation + CPP-DOPA-ON treatment, V: RAW264.7 macrophages after RANKL stimulation + Lipo/ON treatment). (a) Fluorescence staining of F-actin (red) and nuclei (blue), scale bar = 400 μm; (b and c) Quantitative analysis of the F-actin area and number; (d) TRAP staining, scale bar = 400 μm; (e) Quantitative analysis of the TRAP-positive osteoclast area; (f) TRAP activity; (g) Protein levels of NFATc1, c-Fos, and CTSK; (h) Semi-quantitative evaluation of the protein levels shown in (g); (i) Heatmap of osteoclastogenesis-related genes. * denotes $p < 0.05$, ** denotes $p < 0.01$ and ns denotes no significance. (For interpretation of the references to colour in this figure legend, the reader is referred to the Web version of this article.)

osteoclastogenesis-related proteins (NFATc1, c-Fos and CTSK) in the cells as determined by the western blotting assay. Subsequent bone resorption assay confirms that CPP-DOPA-ON effectively inhibits the bone resorption function of osteoclasts (Fig. S5). Based on the above results, we further collect the RANKL-induced macrophages with or without the CPP-DOPA-ON treatment for high-throughput RNA sequencing. The results show a relatively low expression of osteoclastogenesis-related genes such as *acp5*, *mmp9*, and *atp6v0d2* of the cells after the CPP-DOPA-ON treatment (Fig. 4i). On the other hand, the same CPP-DOPA-ON treatment has little influence on the osteogenic differentiation and extracellular matrix (ECM) mineralization of osteoblasts (Figs. S6–8). Hence, CPP-DOPA-ON is demonstrated to suppress osteoclastogenesis without impairing osteogenesis *in vitro* boding well for the treatment of osteoporosis.

3.5. Transcriptome sequencing of CPP-DOPA-ON for osteoclastogenesis

The underlying mechanism of how CPP-DOPA-ON affects osteoclastogenesis is explored by the transcriptome sequencing analysis. The RAW 264.7 cells induced by RANKL constitute the control, and those in treatment group are incubated with CPP-DOPA-ON for 12 h prior to RANKL induction. The cells of both groups are collected for high-throughput sequencing. The volcano plots of differentially expressed genes (DEGs) indicate 1078 up-regulated genes and 824 down-regulated genes after the CPP-DOPA-ON treatment (Fig. 5a). The heatmap reveals significant differences in the DEG expression between these two groups, suggesting that the CPP-DOPA-ON treatment affects the gene expression of induced osteoclasts (Fig. 5b). The principal component analysis (PCA) shows that both samples meet the requirements of quality control (Fig. 5c). The sequencing data are subjected to the Kyoto Encyclopedia of Genes and Genomes (KEGG) enrichment analysis to study the potential signaling pathways. The results demonstrate that the gene expressions related to MAPK signaling pathways and osteoclast differentiation are in top 20 of KEGG pathway enrichment (Fig. 5d). Gene Ontology (GO) enrichment is also performed to explore the differences in the biological functions, which reveals that the biological function of response-to-stress is regulated (Fig. 5e). The sequencing data are investigated by gene set enrichment analysis (GSEA) (Fig. 5f). Consistent with the KEGG results, significant enrichment of the pathway of osteoclast differentiation is observed to be down-regulated in the CPP-DOPA-ON group. In addition, the gene enrichment of type I interferon (IFN) response and hallmark of the IFN alpha response are up-regulated after the CPP-DOPA-ON treatment (Fig. 5g and h). We then analyze the type I IFN response gene set from the sequencing data and identify the significantly increased genes in the treatment group. Previous studies have shown that the interferon pathway plays an important inhibitory role in osteoclast differentiation. IFN-β signaling can be induced by RANKL and up-regulated by the protein kinase double-stranded RNA-dependent (PKR), which is critical to maintaining the balanced differentiation state of osteoclasts [23,31–33]. In line with previous studies, Fig. 5i reveals that the CPP-DOPA-ON treatment up-regulates the expression of Eif2ak2 (encodes PKR). The above results disclose the mechanisms and practical effects of CPP-DOPA-ON on osteoclastogenesis suppression.

3.6. ROS scavenging capability of CPP-DOPA-ON

Osteoclastogenesis is associated with increased levels of ROS, which can promote mature osteoclast formation and bone resorption under osteoporotic conditions. Therefore, ROS scavenging is an effective way to suppress osteoclastogenesis. Since the CPP-DOPA-ON sequence contains several DOPA groups with anti-oxidation effects, it is speculated to scavenge the overexpressed ROS in association with the development of osteoporosis. As shown by the flow cytometry results in Fig. 6a, the percentage of ROS-positive cells induced by RANKL decreases from 85.0 % in the control group to 63.8 % after the CPP-DOPA-DBCO treatment and 61.7 % after the CPP-DOPA-ON treatment, attributable to the presence of DOPA groups in both samples. The levels of ROS expression in the different groups are examined by fluorescence microscopy. When a relatively high level of ROS expression is observed from the control group, the ROS fluorescence intensity of the cells after CPP-DOPA-DBCO or CPP-DOPA-ON treatment decreases significantly (Fig. 6b and c), whereas the ROS scavenging capability of Azido-ON is limited. Recent studies have found that RANKL-mediated ROS/Keap1/Nrf2 signaling axis plays an important role in osteoclastogenesis. As a redox-sensitive transcription factor, Nrf2 regulates the expression of multiple antioxidant enzymes [34,35]. To investigate the mechanism, the expressions of Nrf2 and downstream proteins are evaluated by western blotting assay. As shown in Fig. 6d–f, the protein expressions of Nrf2, SOD2, and HO-1 (other antioxidant enzymes) in the CPP-DOPA-DBCO and CPP-DOPA-ON groups are higher than those of the other groups. Collectively, CPP-DOPA-ON can suppress ROS generation by the antioxidant properties of DOPA groups and enhance ROS scavenging *via* the ROS/Keap1/Nrf2 signaling axis. By considering the cell penetrating capability of CPP, ROS scavenging effects of DOPA, and anti-osteoclastogenesis of ON, CPP-DOPA-ON has great potential in the treatment of osteoporosis.

3.7. In vivo performances of CPP-DOPA-ON

Encouraged by the excellent results obtained from CPP-DOPA-ON *in vitro*, the therapeutic effects are evaluated *in vivo* using osteoporotic mice as the animal model. The experimental mice are divided randomly into four groups and treated as follows: (1) Healthy mice treated by phosphate buffer solution (PBS) as the Sham group, (2) Ovariectomized (OVX) mice treated by PBS as the OVX group, (3) OVX mice treated by Azido-ON as the Azido-ON group, and (4) OVX mice treated by CPP-DOPA-ON as the CPP-DOPA-ON group. Starting from the 31st day post-surgery, the mice are injected intravenously twice a week for 4 weeks and the therapeutic effects are monitored by micro-CT scanning and histological analysis (Fig. 7a). As shown by the micro-CT and 3D reconstructed images in Fig. 7b, OVX surgery induces osteoporotic bone loss in experimental mice and the CPP-DOPA-ON treatment ameliorates the osteoporotic conditions after OVX surgery. Compared with the OVX group and Azido-ON group, the CPP-DOPA-ON group shows higher bone volume per total volume (BV/TV), bone surface per total volume (BS/TV), and trabecular number (Tb. N) as well as smaller trabecular separation (Tb. Sp), indicating better osteogenesis after the CPP-DOPA-ON treatment (Fig. 7c–f). To further investigate the therapeutic effects of CPP-DOPA-ON, the femoral samples harvested from different groups are examined by hematoxylin-eosin (H&E) staining and TRAP staining. As shown in Fig. 7g, the amount of cancellous bone is the smallest in the OVX group, and CPP-DOPA-ON treatment increases the amount of cancellous bone. In addition, the CPP-DOPA-ON group shows a smaller number of TRAP-positive cells in the osteoporotic femoral condyle than the OVX group (Fig. 7h and i). Concomitantly, CPP-DOPA-ON has limited effect on new bone formation (Fig. S9). These encouraging results indicate that the CPP-DOPA-ON therapy is effective in alleviating the osteoporotic condition *in vivo*.

Owing to the inferior capability of bone regeneration, it is more difficult for osteoporotic patients to obtain stable bone-implant integration after bone surgery. The continuous progression of osteoporosis may compromise the quality of the human skeleton and increase the risk of implant loosening and failure. In this respect, the normal and osteoporotic animals are introduced with femoral defects after implantation of Ti, and different treatments are performed 3 days later (Fig. 8a). As shown by the micro-CT scanning and 3D reconstruction results in Fig. 8b, peri-implant bone regeneration of the osteoporotic mice improves significantly after the CPP-DOPA-ON treatment. The bone morphometric parameters measured in the CPP-DOPA-ON group are superior to those of the OVX group (Fig. 8c–g). In addition to micro-CT, histological analysis validates the effects of CPP-DOPA-ON in

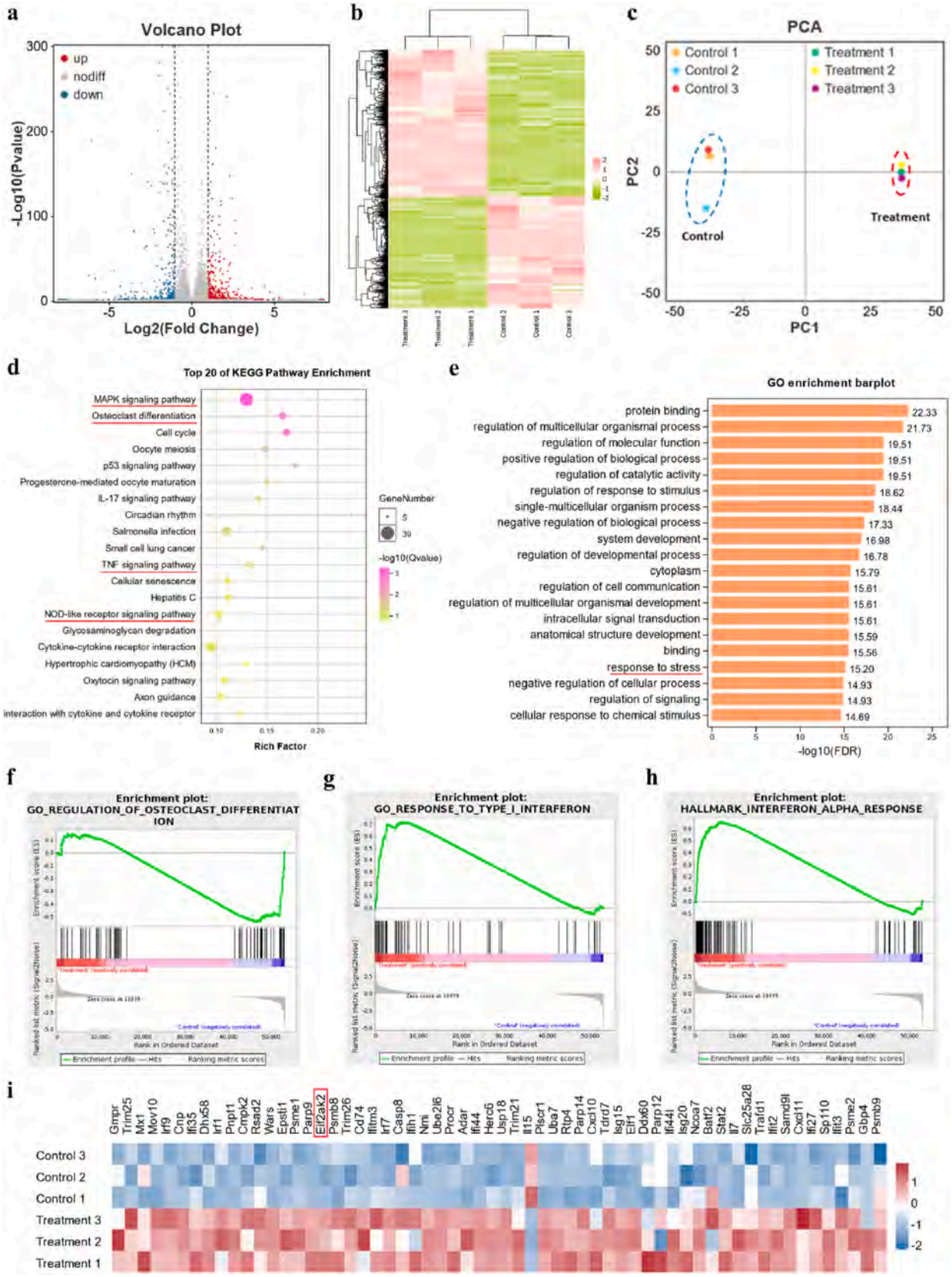

Fig. 5. Transcriptome sequencing analysis of osteoclasts with or without the CPP-DOPA-ON treatment. (a) Volcano map of all the genes between the 2 groups; (b) Heatmap of all the gene expressions; (c) PCA results; (d) KEGG enrichment analysis; (e) GO enrichment analysis; (f–h) GSEA results of osteoclast differentiation (f), type I IFN response (g), and hallmark of IFN alpha response (h); (i) Heatmap of the enriched genes up-regulated by the CPP-DOPA-ON treatment in the type I IFN response signaling pathway.

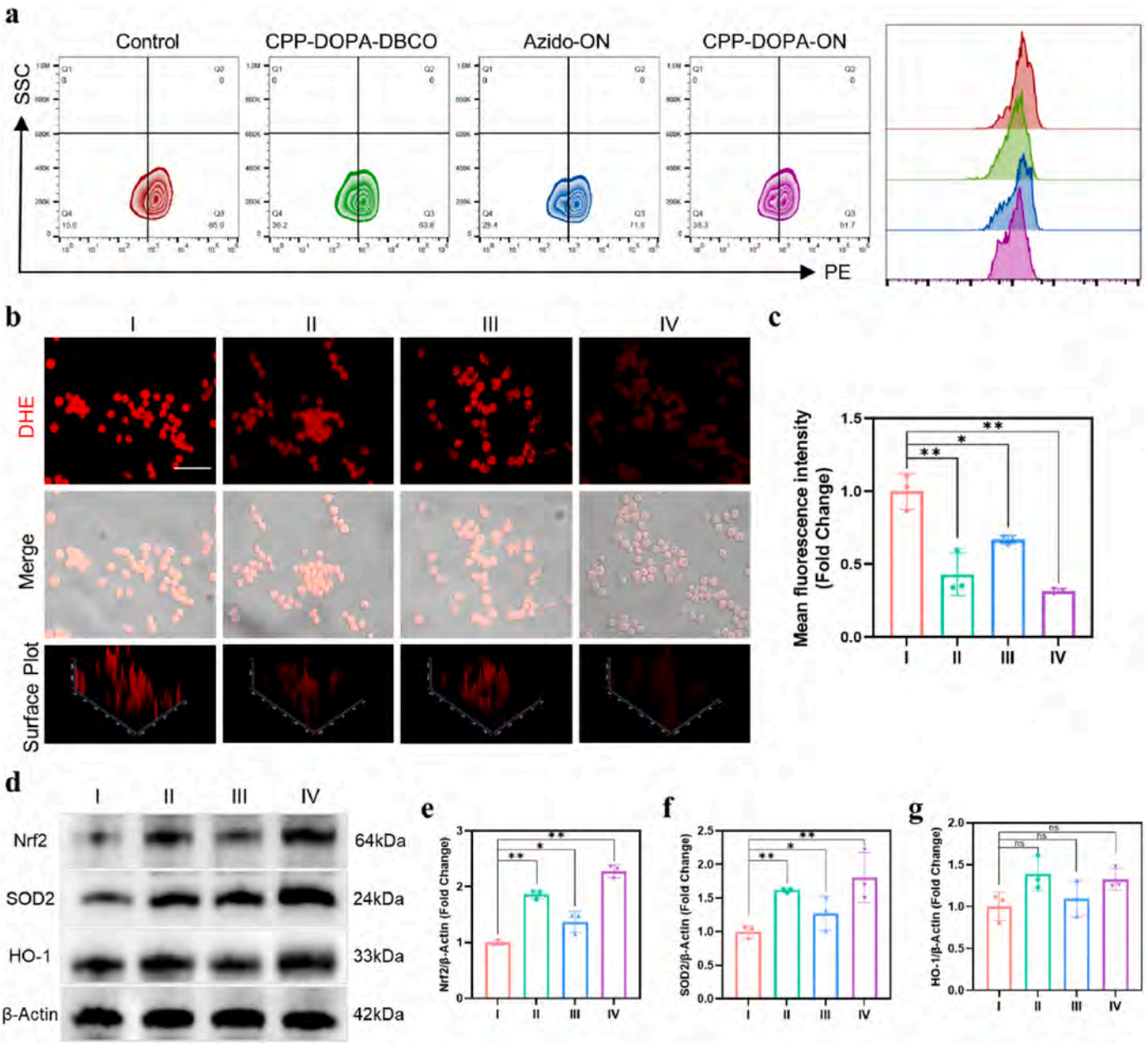

Fig. 6. ROS scavenging capability of different samples (I: RAW264.7 macrophages after RANKL stimulation, II: RAW264.7 macrophages after RANKL stimulation + CPP-DOPA-DBCO treatment, III: RAW264.7 macrophages after RANKL stimulation + Azido-ON treatment, IV: RAW264.7 macrophages after RANKL stimulation + CPP-DOPA-ON treatment). (a) Flow cytometry analysis of ROS-positive cells; (b) ROS fluorescence staining of the cells (scale bar = 50 μm); (c) Quantitative analysis of ROS fluorescence staining; (d) Protein levels of Nrf2, SOD2, and HO-1; (e–g) Semi-quantitative evaluation of the protein levels shown in (d). * denotes $p < 0.05$, ** denotes $p < 0.01$ and ns denotes no significance.

ameliorating osteoporosis. As shown in Fig. 8h, a thick fibrous layer with abundant inflammatory cells is detected from the peri-implant tissue of the OVX group. In contrast, the CPP-DOPA-ON group shows a larger bone mass and less fibrous hyperplasia (Fig. 8h). The number of peri-implant osteoclasts of the CPP-DOPA-ON group is less than that of the OVX group (Fig. 8i and j) and is even close to that detected from the Sham Group. With regard to the serum levels of TRAP and β-CTx, a similar trend can be found (Figs. S10 and S11). On the other hand, the same CPP-DOPA-ON treatment has little influence on new bone formation, which is confirmed by the detection of serum PINP levels (Fig. S12) and histologic sections after Masson staining (Fig. S13). These results provide evidence that the CPP-DOPA-ON treatment reduces further loss of osteoporotic bone around the Ti implants by inhibiting excessive osteoclastogenesis.

Finally, the major organs (heart, liver, spleen, lung, and kidney) of experimental mice are extracted and subjected to H&E staining. The results show that no obvious morphological abnormalities among the different groups (Fig. S14). Moreover, to assess the biosafety, the serum is harvested and analyzed. As shown in Fig. S15, there is no significant difference in the biochemical indexes: aspartate transaminase (AST), alanine transaminase (ALT), creatinine (CREA), urea, lactic dehydrogenase (LDH), and creatine kinase (CK), thereby corroborating that CPP-DOPA-ON has excellent biosafety *in vivo*.

4. Conclusion

A novel hybrid peptide is designed and fabricated by the bio-orthogonal strategy. Azido-ON and CPP-DOPA-DBCO are synthesized

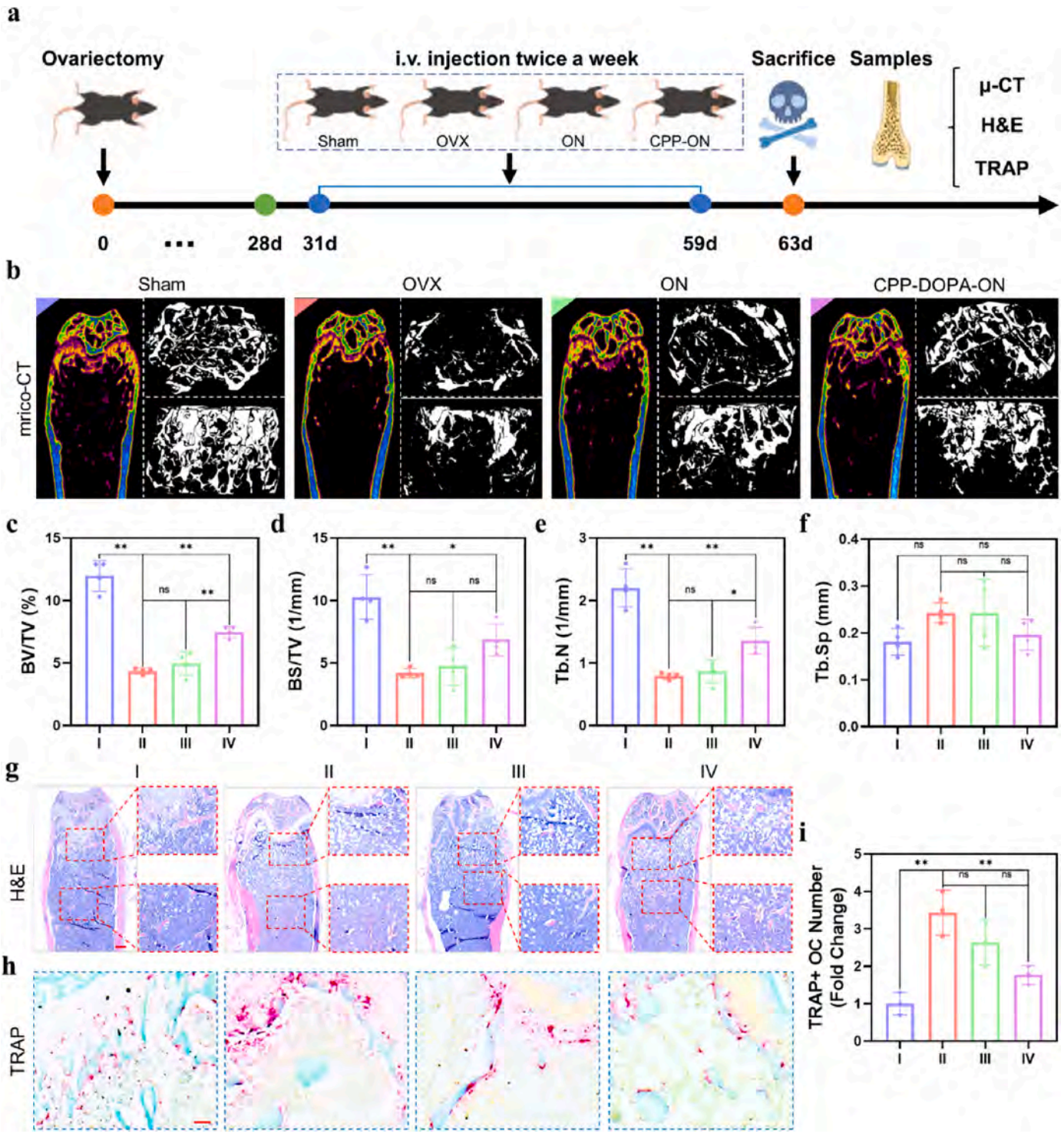

Fig. 7. *In vivo* effects of different treatments on osteoporosis (I: Sham group, II: OVX group, III: Azido-ON group, IV: CPP-DOPA-ON group). (a) Schematic diagram of the animal experiments; (b) Representative images of micro-CT and 3D reconstruction; (c–f) BV/TV, BS/TV, Tb. N and Tb. Sp in the regions of distal femurs; (g) Representative images of distal femurs after H&E staining, scale bar = 200 μm; (h) Representative images of distal femurs after TRAP staining, scale bar = 50 μm; (i) Quantitative analysis of the TRAP-positive cells in distal femurs. * denotes $p < 0.05$, ** denotes $p < 0.01$ and ns denotes no significance.

and the specific click reaction between the Azido and DBCO groups leads to conjugation with a ratio of 1:1. CPP-DOPA-ON is demonstrated to deliver multi-faceted functionalities including cell penetration, lysosome escape, ROS scavenging, and osteoclastogenesis suppression, rendering it effective in the treatment of osteoporosis and postsurgical recovery of osteoporotic fracture after bone implantation. Our study for the first time validates the feasibility of osteoporosis therapy *via* CPP-mediated gene delivery and the results provide insights into the materials design for future biomedical applications.

Author contribution

Conceptualization: Jiaxiang Bai, Huaiyu Wang, Dechun Geng, Methodology: Wei Wang, Qing Wang, Lei Yu, Investigation: Wei Wang,

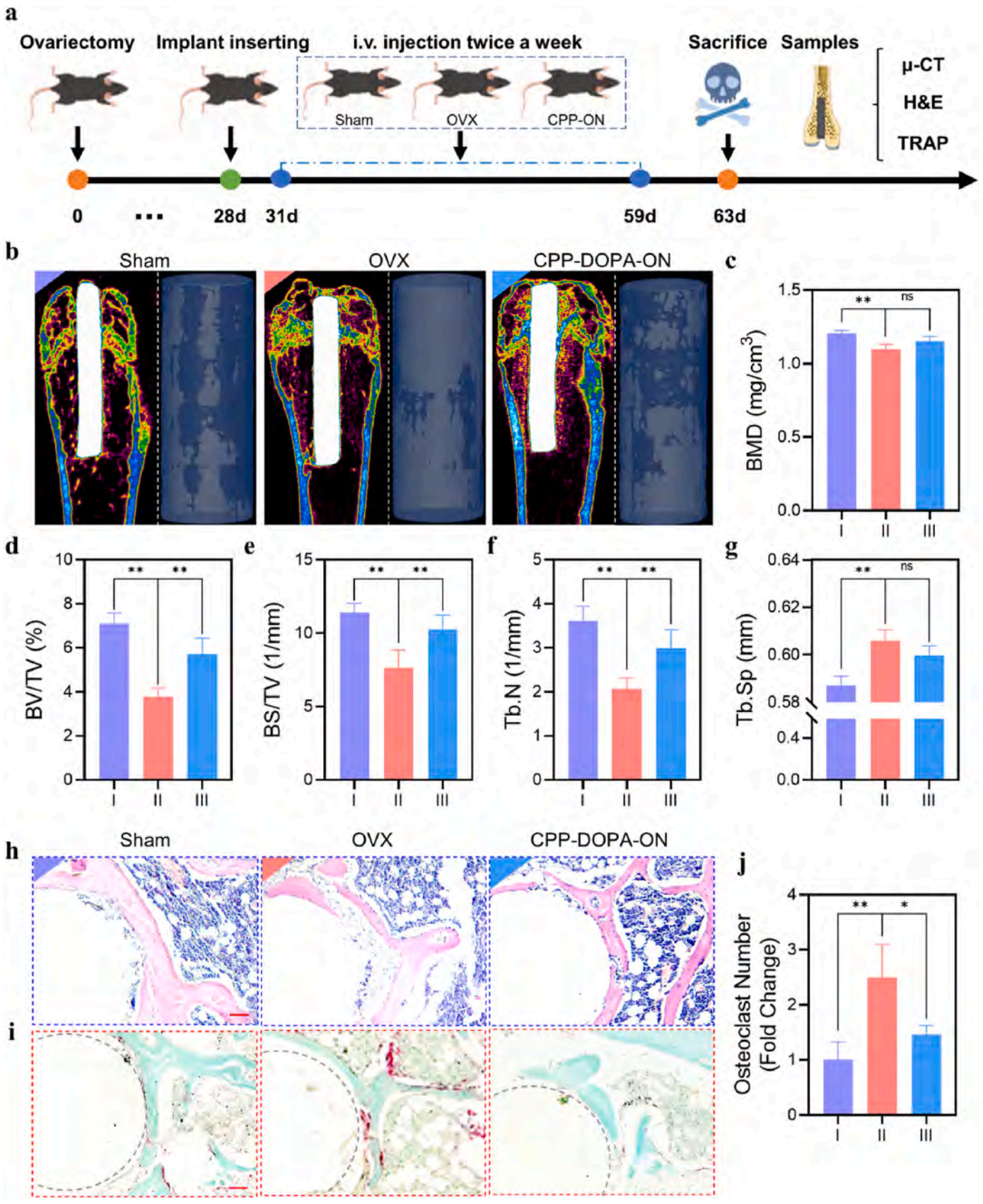

Fig. 8. *In vivo* effects of different treatments on osteoporotic bone implantation (I: Sham group, II: OVX group, III: CPP-DOPA-ON group). (a) Schematic diagram of the animal experiments; (b) Representative images of micro-CT and 3D reconstruction; (c–g) Bone mineral density (BMD), BV/TV, BS/TV Tb. N and Tb. Sp in the peri-implant regions; (h) Representative images of the peri-implant regions after H&E staining, scale bar = 50 μm; (i) Representative images of the peri-implant regions after TRAP staining, scale bar = 50 μm; (j) Quantitative evaluation of the TRAP-positive cells in the peri-implant regions. * denotes $p < 0.05$, ** denotes $p < 0.01$ and ns denotes no significance.

Qing Wang, Lei Yu, Gaoran Ge, Xin Liu, Ang Gao, Supervision: Jiaxiang Bai, Huaiyu Wang, Dechun Geng, Discussion: Guomin Wang, Zhengwei Wu, Writing – original draft: Wei Wang, Qing Wang, Lei Yu, Writing – review & editing: Jiaxiang Bai, Huaiyu Wang, Dechun Geng, Paul K. Chu

Declaration of competing interest

The authors declare that they have no known competing financial interests or personal relationships that could have appeared to influence the work reported in this paper.

Data availability

Data will be made available on request.

Acknowledgements

This work was supported by the National Natural Science Foundation of China (82072425, 82072498, 82272157), Natural Science Foundation of Jiangsu Province (BK2021650), Priority Academic Program Development of Jiangsu Higher Education Institutions (PAPD), Jiangsu Medical Research Project (ZD2022014), Special Project of Diagnosis; Treatment Technology for Key Clinical Diseases in Suzhou (LCZX202003), Program of Suzhou Health Commission (GSWS2022002), National and Local Engineering Laboratory of New Functional Polymer Materials (SDGC2205), China, Shanghai Natural Science Foundation (23ZR1467100), the National Postdoctoral Program for Innovative Talents (BX20230357), the Foundation of National Center for Translational Medicine (Shanghai) SHU Branch (No. SUITM-202301), City University of Hong Kong Donation Research Grants (DON-RMG 9229021 and 9220061), City University of Hong Kong Strategic Research Grant (SRG 7005505), Hong Kong PDFS - RGC Postdoctoral Fellowship Scheme (PDFS2122-1S08 and CityU 9061014), as well as Hong Kong HMRF (Health and Medical Research Fund) (2120972 and CityU 9211320).

Appendix A. Supplementary data

Supplementary data to this article can be found online at https://doi.org/10.1016/j.biomaterials.2023.122352.

References

[1] G. Ballane, J.A. Cauley, M.M. Luckey, G. El-Hajj Fuleihan, Worldwide prevalence and incidence of osteoporotic vertebral fractures, Osteoporos. Int. 28 (5) (2017) 1531–1542.
[2] R.M. Arceo-Mendoza, P.M. Camacho, Postmenopausal osteoporosis: latest guidelines, Endocrinol Metab. Clin. N. Am. 50 (2) (2021) 167–178.
[3] B.F. Boyce, Z. Yao, Q. Zhang, R. Guo, Y. Lu, E.M. Schwarz, L. Xing, New roles for osteoclasts in bone, Ann. N. Y. Acad. Sci. 1116 (2007) 245–254.
[4] J.A. Kanis, O. Johnell, A. Oden, I. Sembo, I. Redlund-Johnell, A. Dawson, C. De Laet, B. Jonsson, Long-term risk of osteoporotic fracture in Malmo, Osteoporos. Int. 11 (8) (2000) 669–674.
[5] Y. Zhang, J. Xu, Y.C. Ruan, M.K. Yu, M. O'Laughlin, H. Wise, D. Chen, L. Tian, D. Shi, J. Wang, S. Chen, J.Q. Feng, D.H. Chow, X. Xie, L. Zheng, L. Huang, S. Huang, K. Leung, N. Lu, L. Zhao, H. Li, D. Zhao, X. Guo, K. Chan, F. Witte, H. C. Chan, Y. Zheng, L. Qin, Implant-derived magnesium induces local neuronal production of CGRP to improve bone-fracture healing in rats, Nat. Med. 22 (10) (2016) 1160–1169.
[6] E.M. Lotz, D.J. Cohen, R.A. Ellis, J.S. Wayne, Z. Schwartz, B.D. Boyan, Ibandronate treatment before and after implant insertion impairs osseointegration in aged rats with ovariectomy induced osteoporosis, JBMR Plus 3 (7) (2019), e10184.
[7] H. Li, Z. Xiao, L.D. Quarles, W. Li, Osteoporosis: mechanism, molecular target and current status on drug development, Curr. Med. Chem. 28 (8) (2021) 1489–1507.
[8] S. Song, Y. Guo, Y. Yang, D. Fu, Advances in pathogenesis and therapeutic strategies for osteoporosis, Pharmacol. Ther. 237 (2022), 108168.
[9] T. Iantomasi, C. Romagnoli, G. Palmini, S. Donati, I. Falsetti, F. Miglietta, C. Aurilia, F. Marini, F. Giusti, M.L. Brandi, Oxidative stress and inflammation in osteoporosis: molecular mechanisms involved and the relationship with microRNAs, Int. J. Mol. Sci. 24 (4) (2023).
[10] T.S. Agidigbi, C. Kim, Reactive oxygen species in osteoclast differentiation and possible pharmaceutical targets of ROS-mediated osteoclast diseases, Int. J. Mol. Sci. 20 (14) (2019).
[11] S. Khosla, L.C. Hofbauer, Osteoporosis treatment: recent developments and ongoing challenges, Lancet Diabetes Endocrinol. 5 (11) (2017) 898–907.
[12] C. Brown, Osteoporosis: staying strong, Nature 550 (7674) (2017) S15–S17.
[13] D. Li, Z. Gao, Q. Li, X. Liu, H. Liu, Cuproptosis-a potential target for the treatment of osteoporosis, Front. Endocrinol. 14 (2023), 1135181.
[14] I.R. Reid, A broader strategy for osteoporosis interventions, Nat. Rev. Endocrinol. 16 (6) (2020) 333–339.
[15] T.C. Roberts, R. Langer, M.J.A. Wood, Advances in oligonucleotide drug delivery, Nat. Rev. Drug Discov. 19 (10) (2020) 673–694.
[16] M. Egermann, E. Schneider, C.H. Evans, A.W. Baltzer, The potential of gene therapy for fracture healing in osteoporosis, Osteoporos. Int. 16 (Suppl 2) (2005) S120–S128.
[17] M. Gao, Z. Zhang, J. Sun, B. Li, Y. Li, The roles of circRNA-miRNA-mRNA networks in the development and treatment of osteoporosis, Front. Endocrinol. 13 (2022), 945310.
[18] L.A. Bravo Vazquez, M.Y. Moreno Becerril, E.O. Mora Hernandez, G.G. Leon Carmona, M.E. Aguirre Padilla, S. Chakraborty, A. Bandyopadhyay, S. Paul, The emerging role of MicroRNAs in bone diseases and their therapeutic potential, Molecules 27 (1) (2021).
[19] Y. Yan, X.Y. Liu, A. Lu, X.Y. Wang, L.X. Jiang, J.C. Wang, Non-viral vectors for RNA delivery, J. Contr. Release 342 (2022) 241–279.
[20] M. Hadjiargyrou, D.E. Komatsu, The therapeutic potential of MicroRNAs as orthobiologics for skeletal fractures, J. Bone Miner. Res. 34 (5) (2019) 797–809.
[21] A. Gupta, J.L. Andresen, R.S. Manan, R. Langer, Nucleic acid delivery for therapeutic applications, Adv. Drug Deliv. Rev. 178 (2021), 113834.
[22] R.L. Setten, J.J. Rossi, S.P. Han, The current state and future directions of RNAi-based therapeutics, Nat. Rev. Drug Discov. 18 (6) (2019) 421–446.
[23] K. Inoue, Z. Deng, Y. Chen, E. Giannopoulou, R. Xu, S. Gong, M.B. Greenblatt, L. S. Mangala, G. Lopez-Berestein, D.G. Kirsch, A.K. Sood, L. Zhao, B. Zhao, Bone protection by inhibition of microRNA-182, Nat. Commun. 9 (1) (2018) 4108.
[24] C.H. Miller, S.M. Smith, M. Elguindy, T. Zhang, J.Z. Xiang, X. Hu, L.B. Ivashkiv, B. Zhao, RBP-J-Regulated miR-182 promotes TNF-alpha-induced osteoclastogenesis, J. Immunol. 196 (12) (2016) 4977–4986.
[25] C. Zhao, J. Chen, J. Ye, Z. Li, L. Su, J. Wang, Y. Zhang, J. Chen, H. Yang, J. Shi, J. Song, Structural transformative antioxidants for dual-responsive anti-inflammatory delivery and photoacoustic inflammation imaging, Angew Chem. Int. Ed. Engl. 60 (26) (2021) 14458–14466.
[26] K. Desale, K. Kuche, S. Jain, Cell-penetrating peptides (CPPs): an overview of applications for improving the potential of nanotherapeutics, Biomater. Sci. 9 (4) (2021) 1153–1188.
[27] G. Guidotti, L. Brambilla, D. Rossi, Cell-penetrating peptides: from basic research to clinics, Trends Pharmacol. Sci. 38 (4) (2017) 406–424.
[28] G. Pan, S. Sun, W. Zhang, R. Zhao, W. Cui, F. He, L. Huang, S.H. Lee, K.J. Shea, Q. Shi, H. Yang, Biomimetic design of mussel-derived bioactive peptides for dual-functionalization of titanium-based biomaterials, J. Am. Chem. Soc. 138 (45) (2016) 15078–15086.
[29] J. Sun, Y. Huang, H. Zhao, J. Niu, X. Ling, C. Zhu, L. Wang, H. Yang, Z. Yang, G. Pan, Q. Shi, Bio-clickable mussel-inspired peptides improve titanium-based material osseointegration synergistically with immunopolarization-regulation, Bioact. Mater. 9 (2022) 1–14.
[30] M.A. Dobrovolskaia, J.D. Clogston, B.W. Neun, J.B. Hall, A.K. Patri, S.E. McNeil, Method for analysis of nanoparticle hemolytic properties in vitro, Nano Lett. 8 (8) (2008) 2180–2187.
[31] H. Takayanagi, S. Kim, K. Matsuo, H. Suzuki, T. Suzuki, K. Sato, T. Yokochi, H. Oda, K. Nakamura, N. Ida, E.F. Wagner, T. Taniguchi, RANKL maintains bone homeostasis through c-Fos-dependent induction of interferon-beta, Nature 416 (6882) (2002) 744–749.
[32] B. Zhao, L.B. Ivashkiv, Negative regulation of osteoclastogenesis and bone resorption by cytokines and transcriptional repressors, Arthritis Res. Ther. 13 (4) (2011) 234.
[33] N. Binder, C. Miller, M. Yoshida, K. Inoue, S. Nakano, X. Hu, L.B. Ivashkiv, G. Schett, A. Pernis, S.R. Goldring, F.P. Ross, B. Zhao, Def6 restrains osteoclastogenesis and inflammatory bone resorption, J. Immunol. 198 (9) (2017) 3436–3447.
[34] D. Chen, Q. Wang, Y. Li, P. Sun, V. Kuek, J. Yuan, J. Yang, L. Wen, H. Wang, J. Xu, P. Chen, Notopterol attenuates estrogen deficiency-induced osteoporosis via repressing RANKL signaling and reactive oxygen species, Front. Pharmacol. 12 (2021), 664836.
[35] Y. Xu, D. Song, Y. Su, J. Chen, L. Wu, H. Lian, N. Hai, J. Li, J. Jiang, J. Zhao, J. Xu, Q. Liu, Pharmacology-based molecular docking of 4-methylcatechol and its role in RANKL-mediated ROS/Keap1/Nrf2 signalling axis and osteoclastogenesis, Biomed. Pharmacother. 159 (2023), 114101.

Supporting Information

Bio-orthogonal engineered peptide: A multi-functional strategy for the gene therapy of osteoporotic bone loss

Wei Wang [a 1], Qing Wang [a 1], Lei Yu [a b 1], Gaoran Ge [a], Xin Liu [a], Ang Gao [c], Guomin Wang [d], Zhengwei Wu [d e], Jiaxiang Bai [a b f], Huaiyu Wang [c*], Paul K Chu [d], Dechun Geng [a*]*

[a] Department of Orthopedics, Medical 3D Printing Center, The First Affiliated Hospital of Soochow University, 188 Shizi Road, Suzhou 215006, Jiangsu, China.

[b] Department of Orthopedics, The First Affiliated Hospital of USTC, Division of Life Sciences and Medicine, University of Science and Technology of China, Hefei, 230022, China.

[c] Center for Human Tissues and Organs Degeneration, Shenzhen Institute of Advanced Technology, Chinese Academy of Sciences, Shenzhen, 518055, China.

[d] Department of Physics, Department of Materials Science and Engineering, and Department of Biomedical Engineering, City University of Hong Kong, Tat Chee Avenue, Kowloon, Hong Kong, China.

[e] School of Nuclear Science and Technology and CAS Key Laboratory of Geospace Environment, University of Science and Technology of China, Hefei, China.

[f] National Center for Translational Medicine (Shanghai) SHU Branch, Shanghai University, Shanghai, China.

[1] These authors contributed equally to this work

* Corresponding authors should be addressed to:
szgengdc@suda.edu.cn (D. Geng),
hy.wang1@siat.ac.cn (H. Wang),
jxbai1995@163.com (J. Bai).

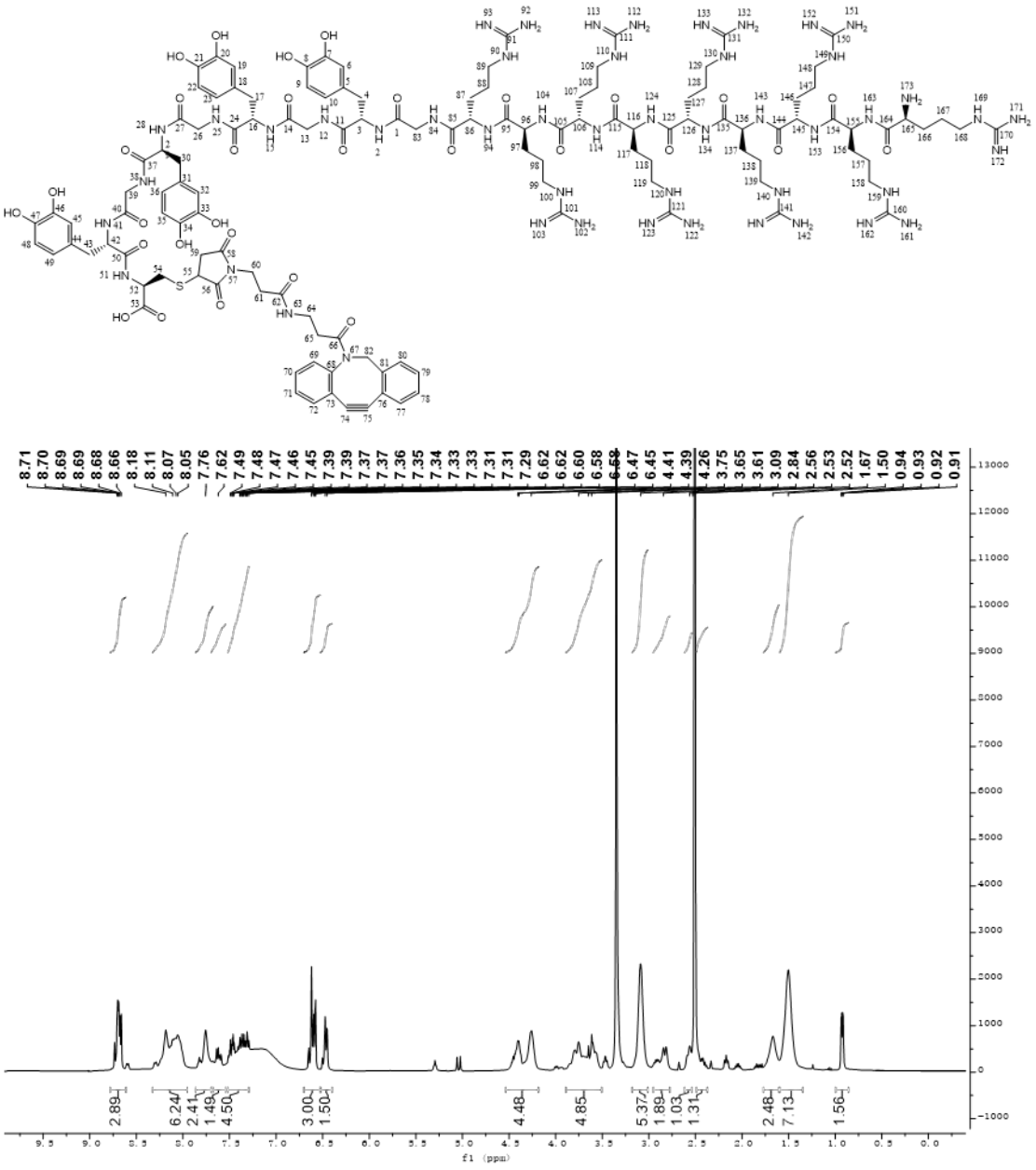

Figure S1. Chemical structure and hydrogen atom number of CPP-DOPA-DBCO.

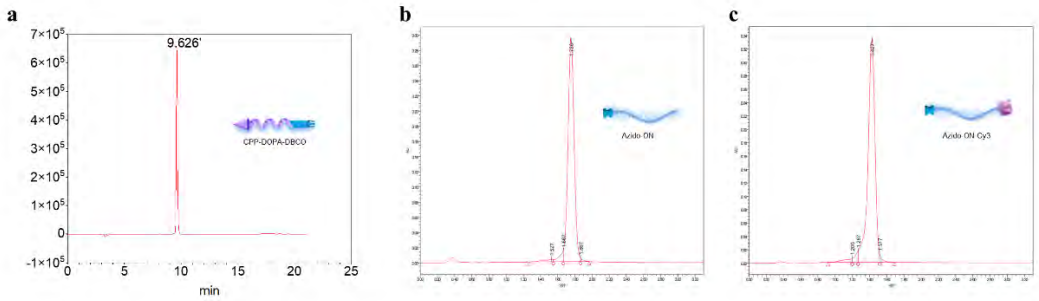

Figure S2. HPLC results: (a) CPP-DOPA-DBCO, (b) Azido-ON, and (c) Azido-ON-Cy3.

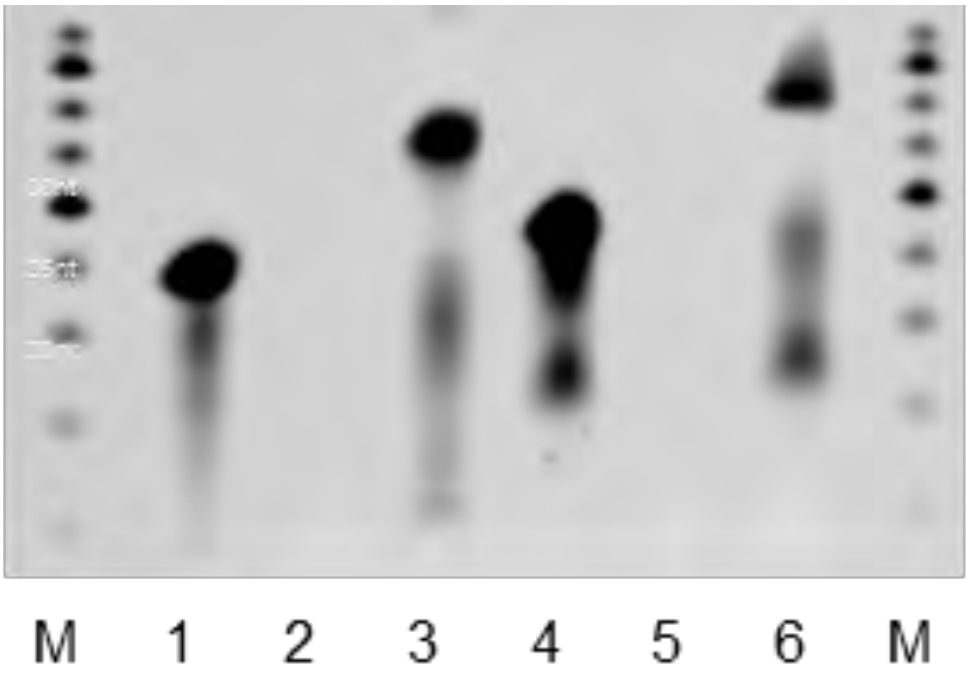

Figure S3. PAGE results: 1: Azido-ON, 2: CPP-DOPA-DBCO, 3: CPP-DOPA-ON, 4: Azido-ON-Cy3, 5: CPP-DOPA-DBCO, 6: CPP-DOPA-ON-Cy3, and M represents the marker.

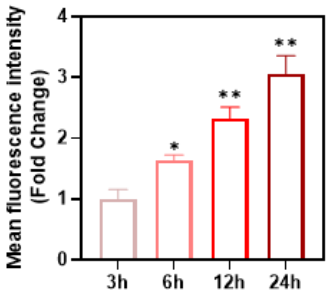

Figure S4. Mean fluorescence intensity of intracellular CPP-DOPA-ON-Cy3 shown in Fig.3b. * denotes $p < 0.05$ and ** denotes $p < 0.01$ compared to the 3h group.

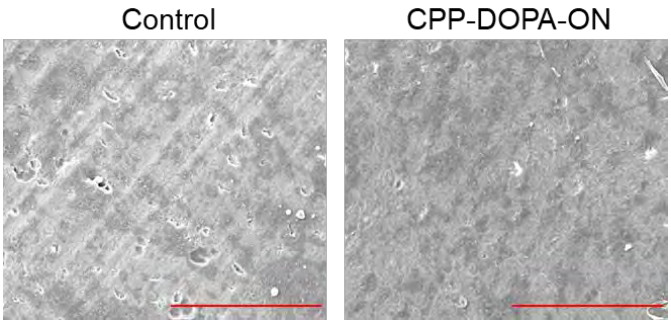

Figure S5. Scanning electron microscopy (SEM) images of bone resorption area with or without CPP-DOPA-ON treatment. Scale bars = 200 μm.

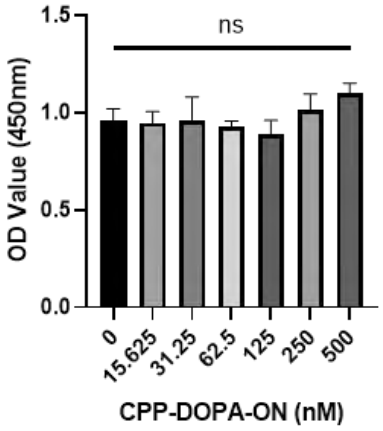

Figure S6. Viability of MC3T3-E1 cells after incubation with CPP-DOPA-ON (0-500 nM) for 2 days. ns denotes no significance compared to the 0 nM group.

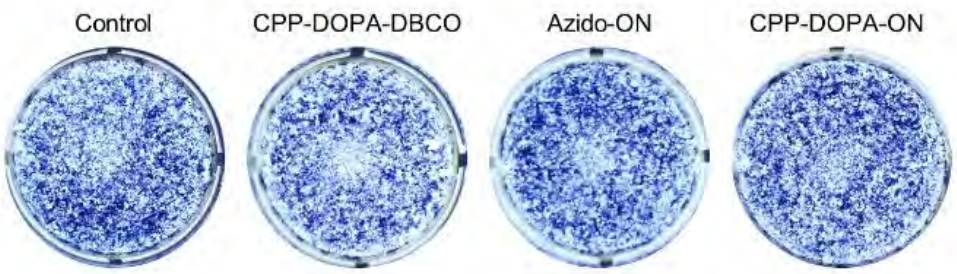

Figure S7. ALP staining images of MC3T3-E1 cells after different treatments.

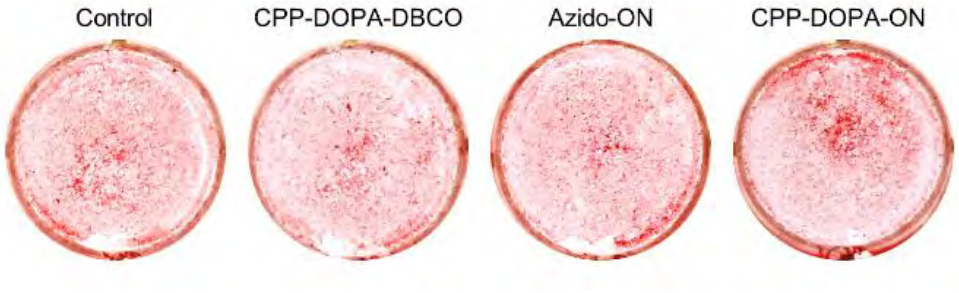

Figure S8. ARS staining images of MC3T3-E1 cells after different treatments.

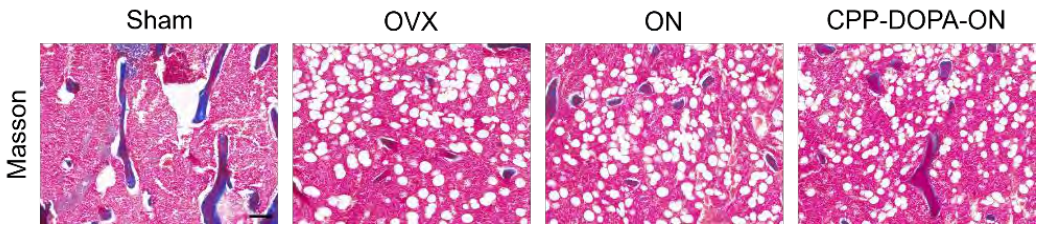

Figure S9. Masson staining of distal femurs of the mice in different groups, scale bar =100 μm.

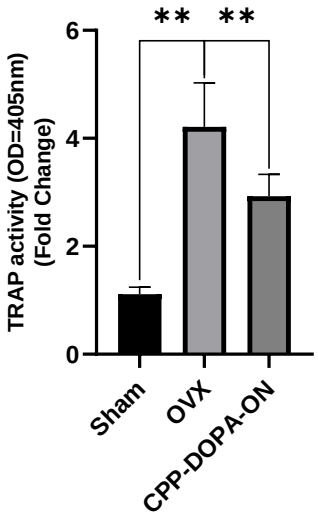

Figure S10. TRAP activity of the serum samples of the mice in different groups, ** denotes $p < 0.01$.

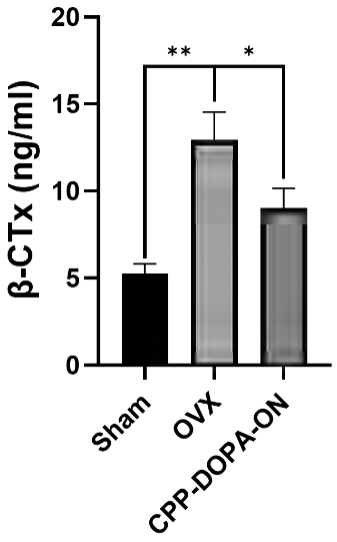

Figure S11. β-CTx level of the serum samples of the mice in different groups, * denotes $p < 0.05$ and ** denotes $p < 0.01$.

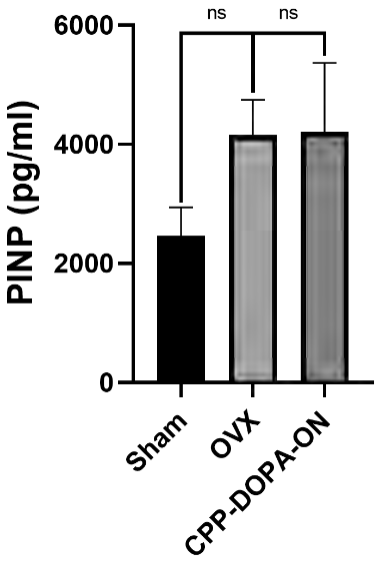

Figure S12. PINP level of the serum samples of the mice in different groups, ns denotes no significance.

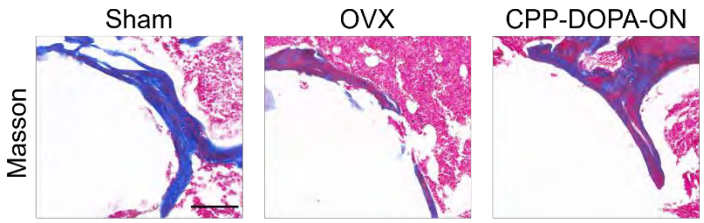

Figure S13. Masson staining of the peri-implant regions of the mice in different groups, scale bar =100 μm.

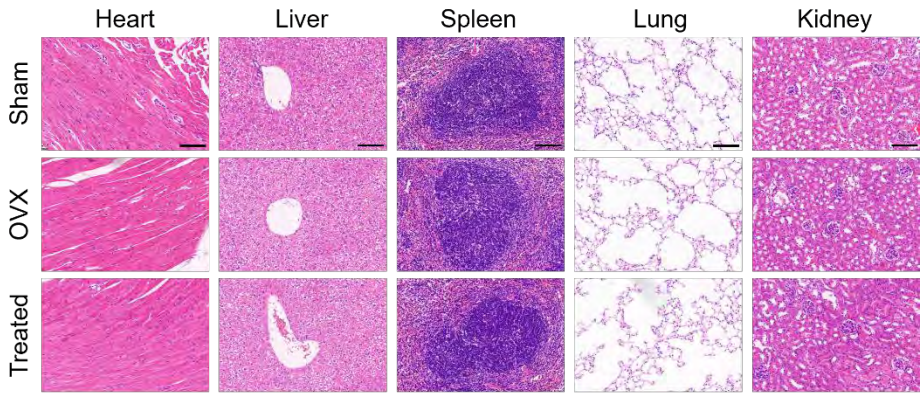

Figure S14. H&E staining of the major organs (heart, liver, spleen, lung and kidney) of the mice in different groups, scale bar = 100 μm.

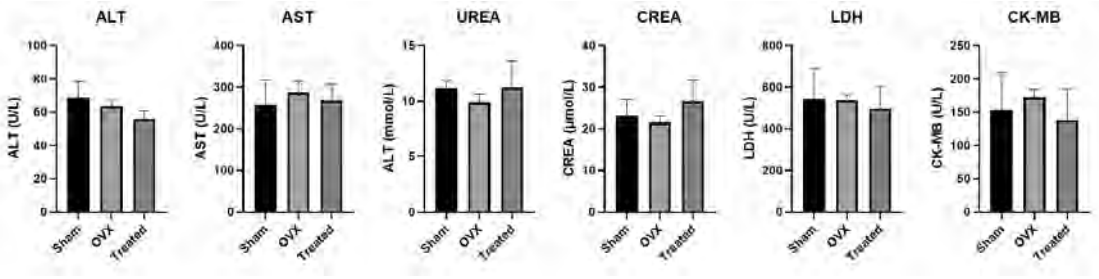

Figure S15. Biochemical and blood routine evaluation of the mice in different groups.